Enhancing the Charge Transport in Solution-Processed Perylene Di-imide Transistors via Thermal Annealing of Metastable Disordered Films

Laura Ferlauto, Fabiola Liscio, Emanuele Orgiu,* Norberto Masciocchi, Antonietta Guagliardi, Fabio Biscarini, Paolo Samorì,* and Silvia Milita*

The introduction of side chains in π-conjugated molecules is a design strategy widely exploited to increase molecular solubility thus improving the processability, while directly influencing the self-assembly and consequently the electrical properties of thin films. Here, a multiscale structural analysis performed by X-ray diffraction, X-ray reflectivity, and atomic force microscopy on thin films of dicyanoperylene molecules decorated with either linear or branched side chains is reported. The substitution with asymmetric branched alkyl chains allows obtaining, upon thermal annealing, field-effect transistors with enhanced transport properties with respect to linear alkyl chains. Branched chains induce molecular disorder during the film growth from solution, effectively favouring 2D morphology. Post-deposition thermal annealing leads to a structural transition towards the bulk-phase for molecules with branched chains, still preserving the 2D morphology and allowing efficient charge transport between crystalline domains. Conversely, molecules with linear chains self-assemble into 3D islands exhibiting the bulk-phase structure. Upon thermal annealing, these 3D islands keep their size constant and no major changes are observed in the organic field effect transistor characteristics. These findings demonstrate that the disorder generated by the asymmetric branched chains when the molecule is physisorbed in thin film can be instrumental for enhancing charge transport via thermal annealing.

1. Introduction

Organic semiconductors (OSCs) have gained considerable attention in the past decade because they can be incorporated in high performing flexible opto-electronic devices by exploiting simple processing methods, thereby opening new avenues towards a novel generation of low-cost and light-weight electronics.[1–9] Some of them have already entered the marketplace by acting as the active layer in organic light-emitting diodes.[10] The major attractive feature of organic semiconductors is the versatility in material design that offer countless possibilities in building molecules with ad-hoc electronic properties suitable for various printable electronic devices.[11,12] The key to success is to synthesize OSCs exhibiting *i)* high charge carriers mobility (μ) and stability in air as well as operational conditions in order to compete with the amorphous silicon technology performances, i.e. $\mu \sim 1$ cm^2 V^{-1} s^{-1}, and *ii)* high solubility in common solvents to be easily processed by low-cost techniques like spin-coating, ink-jet printing and soft lithography.[13] However, materials possessing all these requirements are still in demand.

The intermolecular interactions between π-conjugated cores are key for an efficient charge transfer between molecules, making the efficiency of charge transport closely related to the extent of molecular order in the bulk material.[14] On the same time, strong intermolecular interactions prevent solvents to dissolve molecules, making the processability difficult. Therefore, the order at the supramolecular level, the processing and

L. Ferlauto, Dr. F. Liscio, Dr. S. Milita
CNR - Istituto per la Microelettronica
e Microsistemi (IMM)
I-40129, Bologna, Italy
E-mail: liscio@bo.imm.cnr.it
Dr. E. Orgiu, Prof. P. Samorì
ISIS & icFRC
Université de Strasbourg & CNRS
8 allée Gaspard Monge
67000, Strasbourg, France
E-mail: orgiu@unistra.fr; Samori@unistra.fr

DOI: 10.1002/adfm.201400789

Prof. N. Masciocchi
Dipartimento di Scienza e Alta Tecnologia
Università dell'Insubria and To.Sca.Lab
via Valleggio 11 I-22100, Como, Italy
Dr. A. Guagliardi
Istituto di Cristallografia – CNR and To.Sca.Lab
via Lucini 3 I-22100, Como, Italy
Prof. F. Biscarini
Dipartimento di Scienze della Vita
Università di Modena e Reggio Emilia
Via Campi 183, 41125, Modena and CNR - Istituto
per lo Studio dei Materiali Nanostrutturati (ISMN)
I-40129, Bologna, Italy

the device performance are strongly intertwined.[15–17] Moreover, in n-type OSCs the air stability can markedly affect the electron transport due to the detrimental effect of the oxygen molecules which degrade μ.[18,19] Among various n-type OSCs, perylene alkyl-diimide derivatives, have been demonstrated to meet several requirements such as air stability, processability and high charge carrier mobility at once.[20–27] The functionalization of the perylene core by cyano groups stabilizes the charge carriers by lowering the energy of the lowest unoccupied molecular orbital (LUMO), preventing the formation of oxygen-related electron traps, and enhancing the solubility by slightly decreasing the core planarity.[19,28] Solubility can be further improved by introducing appropriate side-chains.[29,30] Branched alkyl side-chains are known to modify the steric hindrance on the periphery of the polyaromatic cores thereby enabling solvation with the solvents from which these materials are crystallized.[29,31] Favourable π–π stacking interactions can be obtained if defined stacking offsets are present, leading to a ca. 3.4–3.5 Å interlayer separation; also in this case, the size, the shape and the polarity of the alkyl residues play a fundamental role.

The capability of supramolecular organization on a surface and the charge transport is affected by introducing chemical (structural) modifications. Variation of the alkyl chain branching point was recently found to be an effective strategy for tuning of molecular packing and enabling high charge transport mobilities.[32] Attaining an improved processability without perturbing electrical properties of a material is nowadays a great challenge.

Here we show that the asymmetry of branched alkyl chains in perylene-diimide derivatives can be used not only to improve the solubility of the molecule in organic solvent, but also to enhance the performance of organic field-effect transistors (OFETs).

In particular, we use two highly soluble alkyl-diimide perylene isomeric derivatives differing in their alkyl side chains shape but neither in size nor in stoichiometry. By applying a multiscale characterization approach (including structural powder and grazing-incidence X-ray diffraction, X-ray reflectivity, atomic force microscopy), we show that the substitution of linear side chains with asymmetric branched chains (without rigid stereochemical control, vide infra) introduces in the system a structural flexibility and consequent disorder. This latter ultimately leads to a different molecular self-assembly at various length scales (i.e. molecular packing and morphology) when molecules are deposited by spin-coating on the dielectric surface. Although disorder is commonly considered detrimental for OFET performance, films based on molecules possessing asymmetric branched alkyl chains grow forming metastable structures which can be modified by a further post-processing annealing step at 110 °C for 5 h and in this way optimized for charge transport leading to a field-effect mobility increase up to 70-fold.

2. Results and Discussion

2.1. The Structures of the Bulk

We focused on *N*′-bis(n-octyl)-dicyanoperylene-3,4:9,10-bis(dicarboxyimide) (PDI8CN2), which is a well-known air-stable n-type OSC featuring mobilities as high as 0.2 $cm^2\ V^{-1}\ s^{-1}$,[26,33–35] and *N,N*′-bis-(2-ethylhexyl)-1,7-dicyanoperylene-3,4:9,10-bis(dicarboxyimide) (N1400), which is an emerging n-type OSC with high processability.[36] Being based on the same perylene core with CN_2 functionalization in the bay area, their chemical structures differ in the type of alkyl chains attached to the nitrogen atom, which are linear and branched for PDI8CN2 and N1400, respectively (see **Figure 1**a,b).

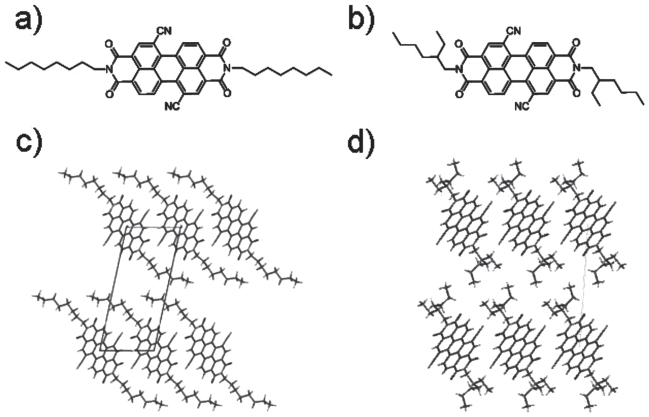

Figure 1. Chemical formula of (a) PDI8CN2 and (b) N1400. Schematic drawings of the crystal structure viewed down [100] of (c) PDI8CN2[34] and (d) N1400. In the latter case, for sake of simplicity, only one of the four possible diastereoisomers (R,S or *meso*), disordered within the crystals, is shown.

The knowledge of the packing features of these molecules within the crystal represents the starting point to understand the charge transport mechanism occurring in OSC. Figures 1c and d show the comparison between the crystal structure of bulk PDI8CN2, taken from ref. [34], and that of N1400. The latter has been here determined by means of ab-initio X-ray powder diffraction methods using a rigid body description for the whole molecule, flexible at the C-C torsion angles of the alkyl residues (Supporting Information includes the details on the rather complex structure determination process of this disordered molecular compound, and the final powder diffraction traces matching shown in Figure S1).

Powder XRD measurements revealed that N1400 self-assembles into triclinic crystals belonging to space group P-1; the cell parameters are a = 6.302(1), b = 8.8095(7); c = 16.557(3) Å, α = 88.322(8), β = 84.60(1), γ = 110.63(1)°. The synthesis of this species, performed by using racemic 2-ethyl-hexylamine in the absence of chiral induction, leads to the formation of a mixture of four stereoisomers, two RR/SS and RS/SR enantiomeric pairs. As detailed in the Supporting Information, the presence of a statistical inversion center (and of a Z′ = 0.5 crystal structure) is a consequence of the disorder of the alkyl branches (R or S, in 50% probability on either side), the overall crystal packing being only marginally affected by the relative disposition of the S (or R) ethyl residues within very flexible alkyl chains. Rather surprisingly, the density of N1400, possessing disordered alkyl chains, is slightly higher than that of the pristine PDI8CN2 species (1.290 vs. 1.281 g cm^{-3}); although uncommon, this effect is not new, as nicely presented nearly 30 years ago in the seminal paper by Bar and Bernstein on conformational polymorphism,[37] in which disorder was considered a stabilizing

effect, contrasting a less favorable molecular conformation. Analogously, the higher compactness of N1400, following Dunitz's observations,[38] indicates the presence of a lower internal energy, possibly linked to an additional entropic contribution granted by alkyl disorder. Indeed, the melting points of the two species (300 °C for PDI8CN2 and 315 °C for N1400) seem to support these observations, i.e. the occurrence of a lower $\Delta G°_f$ value for N1400 (under the assumption that their liquids possess similar thermodynamic stability).

Substituted perylene tetracarboxylic diimides tend to tightly pack with closely stacked cores at distances typically lying in the 3.40–3.50 Å range:[39] PDI8CN2 molecules are separated by 3.40 Å, while in N1400 the distance among parallel polyaromatic cores is slightly increased (up to 3.54 Å). The two structures also differ in the relative offsets, which (as shown in Figure S2) can be quantitatively assessed by the angle between the a axis (the shortest translation) and the longest N–N vector within polyaromatic moiety: 46.3° in PDI8CN2 and 34.6° in N1400 (0° corresponding to perfectly eclipsed polyaromatic cores). Different stacking modes can indeed occur in closely related species as evidenced by Brédas et al., who extensively modeled by first-principle methods the energetics of the π–π interaction upon molecular shifts along two (mutually perpendicular) axes for strictly parallel cores set 3.40 Å apart.[40]

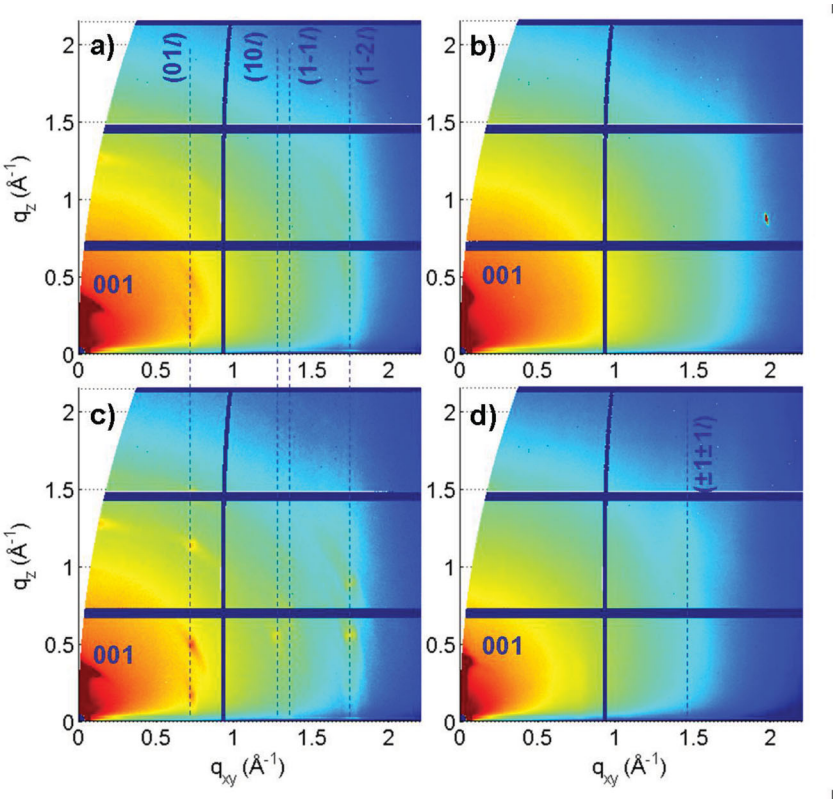

Figure 2. 2D-GIXRD images at incident angle 0.1° of thin-films spin-coated on HMDS-treated substrates. As-cast: a) PDI8CN2, and b) N1400. Thermal treated at 110 °C for 5 hours: c) PDI8CN$_2$, and d) N1400. All the images have the same intensity log-scale.

Interestingly, solubility measurements of the two materials in chloroform ($CHCl_3$) give different results: 2 mg/mL for PDI8CN2 and 5 mg/mL for N1400. Despite the identical molecular weights, and the similar shape and crystal packing features, we can tentatively attribute this finding to two concurring effects: *i)* the branched nature of the 2-ethyl-hexyl residues (known to surpass, in enhancing solubility, linear alkyls),[41] and *ii)* the occurrence of multiple "distinct" stereoisomers, which determine anomalously high solubility levels, as if thermodynamically independent components were present. The second effect is analogously found in conglomerates of enantiomorphic crystals[42] and atropisomeric molecules stabilized by hindered rotations.[43]

2.2. The Structures of the Films

A number of films of PDI8CN2 and N1400 were prepared as described in the Experimental section, and characterized structurally, and, later, in their electrical functional properties. Specifically, 2D-Grazing incidence X-ray diffraction (GIXRD) measurements were performed on films prepared by spin-coating a 1.9 mg/mL solution of PDI8CN2 or N1400 from chloroform onto a hexamethyldisilazane (HMDS)-treated SiO_x surface, in order to investigate the effect of the substrate-adsorbate interaction during the film formation. The silicon oxide surface was silanized in order to prevent charge trapping arising from the hydroxyl groups.[44] Although the two structures show some similarities in the bulk, the presence of branched side chains in N1400 hinders the crystallization process. This is witnessed by the larger amount of (weak) Bragg spots observed in the 2D-GIXRD images collected for the PDI8CN2 film (**Figure 2**a) with respect to those collected for the N1400 film (Figure 2b).

By indexing Bragg spots, we can establish that PDI8CN2 films grow according to a 2D-powder-like structure adopting edge-on packing where π–π stacking is lying parallel to the film plane. From the Bragg spots positions the same cell parameters of the bulk phase are extracted,[34] in the limit of the technique resolution. This similarity is related to the pronounced thermodynamic stability of the PDI8CN2 crystal structure which prevents the formation of a (distinct) thin-film phase induced by the substrate interaction, as already shown for evaporated films,[34] even during fast and non-equilibrium grown process as spin casting.[45]

On the other hand, only one Bragg spot is observed in the 2D-GIXRD image collected for the N1400 film (Figure 2b). This spot corresponds to the (001) reflection, which, being in the out-of-plane direction (q_z), reveals that molecules are oriented with their longer axis almost normal to the surface, as found for the PDI8CN2 (i.e. ab plane parallel to the surface). The position of (001) gives a d_{001} spacing value, i.e. the monolayer thickness, equals to 18 Å, more than 1 Å higher than the bulk value, i.e.

d_{001}(*bulk*) = 16.46 Å. The higher monolayer thickness could be ascribed to *i)* a tilting of the average polyaromatic molecular planes towards c*, the normal to the film surface (the ab plane), or *ii)* a tilting and/or a stretching of the alkyl chains. Moreover, no trace of (even partial) crystallinity in the in-plane structure, dominated by the π–π stacking, is observed.

Figure 2c,d report the 2D-GIXRD images recorded after annealing the samples at 110 °C for 5 h. The intensity of Bragg peaks increases in both films, providing evidence for an increased crystallinity as induced by the thermal treatment. In the case of PDI8CN2, the lateral size of the crystallites, evaluated from the peak width along q_{xy} direction, using the Scherrer formula[46] and taking into account the beam footprint as described in ref. [47], increases from 8 to 14 nm. In the case of N1400 a new, very weak Bragg rod appears after annealing (Figures 2d), again assigned to the growth of larger coherent domains in ab. Moreover, after annealing d_{001} decreases towards the bulk phase value (17 Å). This structural transition is more pronounced for a thicker N1400 film, where several Bragg spots appear after the annealing (Figure S3). From those peaks positions, cell parameters close to the bulk phase were deduced. These findings suggest that during the fast spin-coating process, N1400 molecules self-organize in a metastable phase with lower crystalline order. The explanation is strictly related with the alkyl chains morphology. Kinetic effects dominate the crystallization process during the spin coating deposition. Since the deposition parameters are the same for both molecules (isomers), the same amount of thermal energy is available for molecular motions. Given that the π–π staking in the crystal structure of both isomers is similar, because of the strong π–π interaction between aromatic cores, the rotational energy barrier of the isomer with branched alkyl chains is expected to be greater than that with linear ones, resulting in slower molecular motions (this effect can be justified by the spherical hindrance of the branched alkyl chains). Therefore, we suppose that under kinetic regime, i.e. a non-equilibrium process, the isomer with branched alkyl chains does not have enough energy and time to self-assemble in the "bulk" structure and a new metastable phase is formed, which is further stabilized by the entropic contribution provided by the conformational disorder of the branched alkyl chains. The presence of a structural disorder is partially healed by thermal annealing treatments, as also confirmed by rocking curves measurements (see Figure S4 in supporting information for details), which leads to a molecular rearrangement towards the bulk phase.

A quantitative analysis of the film microstructure was performed by carrying out X-ray reflectivity (XRR) measurements on films prepared from solutions with different concentrations (from 0.2 to 1.9 mg/mL). The XRR curves recorded for PDI8CN2 and N1400 films before and after annealing are displayed in **Figure 3**a and b, respectively.

Apart from the N1400 film at the lowest concentration, all XRR curves reveal the presence of the (001) Bragg peak, which

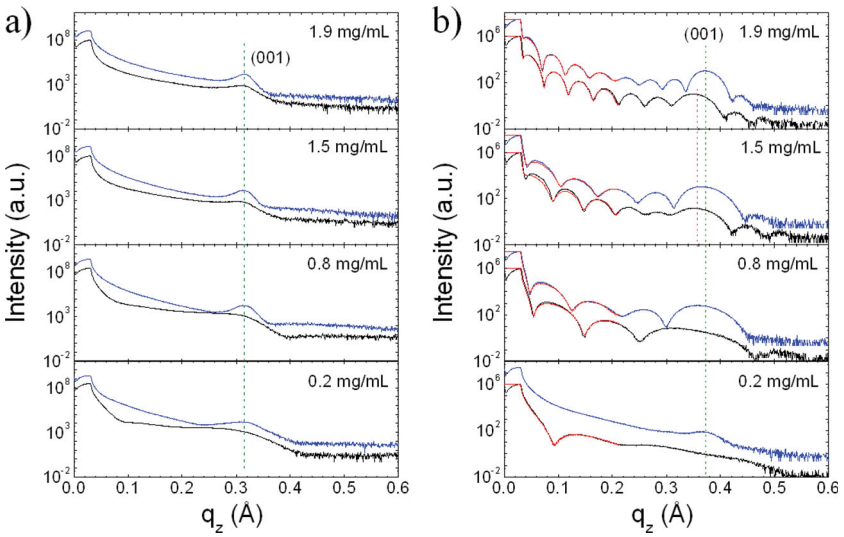

Figure 3. XRR curves collected for (a) PDI8CN$_2$ and (b) N1400 films prepared at various concentrations. Black and blue lines are the data from the as-cast and the annealed film, respectively. Red lines are the fitting curves of Kissieg fringes. Dashed vertical lines indicate the (001) peak position before and after annealing.

progressively intensifies and narrows upon annealing, due to the growth of the crystalline domains along the film thickness, similar to what observed in the 2D-GIXRD experiments for the lateral crystallite dimension. After annealing, the peak position does not change for PDI8CN2 films, whereas it shifts toward the bulk value for N1400 films, confirming the occurrence of the thermally activated phase transition claimed from 2D-GIXRD analysis. The evidence of molecular rearrangement in N1400 films is particularly significant for the film grown from the lowest concentration, where the (001) reflection appears only after annealing.

XRR curves also contain information about the film morphology. The Kiessig fringes, i.e. the oscillations observed at low momentum transfer, are characteristic of a film with a rather smooth surface, and its frequency is directly proportional to the film thickness.[48,49] By fitting these oscillations until q_z = 0.2 Å^{-1}, making use of a single-layer model on top of the substrate within the Parratt formalism,[49,50] the thickness and surface roughness (σ_{surf}) values were extracted (see Table S1 and more details in Supporting Information). For all PDI8CN2 films XRR curves do not show Kissieg fringes, highlighting a 3D island growth with a σ_{surf} above several nanometres, therefore undetectable by XRR. Conversely, N1400 films are characterized by surfaces with roughnesses on the order of a few Å only. Film thickness linearly increases with concentration (from 2.9 nm to 12 nm) due to the larger amount of molecules deposited on the surfaces during the casting. When films are annealed, σ_{surf} slightly increases. This variation is more pronounced at the lowest concentration, where Kissieg fringes disappear after annealing, suggesting a transition from 2D to 3D morphology.

2.3. The Morphology of the Films

The microstructure of the films was corroborated by analysing the atomic force microscopy (AFM) images recorded for all

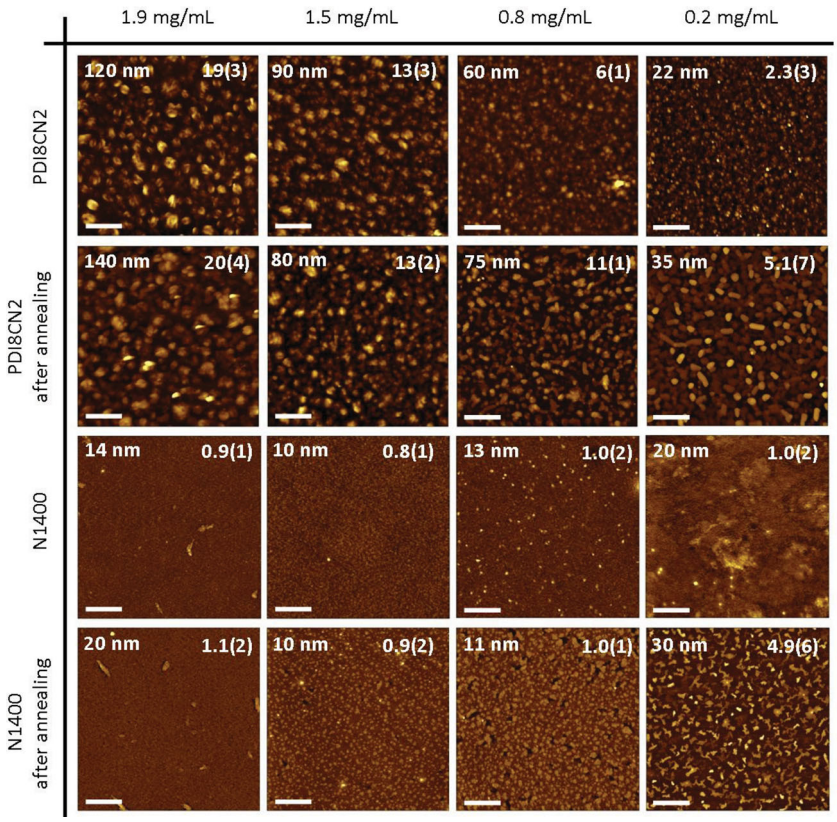

Figure 4. AFM images of spin-coated samples at different concentrations of PDI8CN2 and N1400 as-cast and annealed. The white ticks at the bottom corresponds to 2 μm. The height of the colour bar (i.e., Z-scale) and σ_{RMS} values, both expressed in nm, are reported as in-set on top-left and top-right, respectively. σ_{RMS} variances are in brackets.

films before and after thermal annealing. The AFM images are collectively reported in **Figure 4**, together with the root mean square roughness (σ_{RMS}) values determined for each film as the standard deviation of the film height distribution averaged over three topographic images with a lateral size of 10 μm. For all the concentrations, AFM images of PDI8CN2 films confirm the presence of 3D islands. These consist of rounded-shape grains of several hundreds of nanometers in size, whose average sizes increase with the concentration from 250 nm to 420 nm (as deduced from the grains analysis reported in Supporting Information, Figure S5). However, they do not appear being drastically modified by the thermal treatment, apart from the [0.2 mg/mL] case, where the lateral size dimension doubles. On the other hand, the morphology of N1400 as-cast films is characterized by very smooth surface whose σ_{RMS}, in the limit of the technique resolution, is comparable with the one extracted from XRR.

Thermal treatment induces a morphological change that depends on concentration. For the [1.9 mg/mL] film, σ_{RMS} and grain size remain constant, whereas, when concentration decreases a dewetting phenomenon appears. Dewetting is a well known process[51] occurring when a thin film grows in a metastable phase and the molecules move upon heating, aggregating in a more stable phase in the form of islands; this process also leads to formation of holes, which later grow to form dewetted regions. The driving force for this process is the minimization of the total energy of the free surfaces of both the film and substrate, as well as of the film-substrate interface. The rate of dewetting accelerates with lowering the film thickness. Therefore, at lowest concentration thermal treatment transforms the 2-ML thick film into well-separated 3D crystallites 20 nm high, where molecules are arranged in bulk phase. When concentration increases, the molecular diffusivity decreases and the dewetting phenomenon decreases.

We tentatively propose that the presence of configurational disorder within the N1400 films (that is, the random occurrence of branched side chains of R or S chirality) can be considered being responsible for the growth of the metastable phase; on the contrary, in the case of PDI8CN2, the limited configurational space that can be explored during film growth induces the formation of a unique (stable) phase, less prone to dewetting.

2.4. Transport Properties of the Films

The influence of all the structural and morphological characteristics on the electrical properties was investigated by recording output and transfer curves of bottom-gate bottom-contact OFETs before and after thermal treatment. **Figure 5** reports the mobility extracted in saturation regime (μ_{sat}) and the threshold voltage (V_{th}) values as a function of devices channel length (L). The electrical measurements of all films are reported in the Supporting Information.

The as-cast PDI8CN2 devices exhibit slightly higher values of μ_{sat} with respect to N1400 ones, because the superior crystalline order observed in these films facilitates the charge carrier transport within the domains. Large and negative V_{th} are observed in the films before the annealing with PDI8CN2 devices, a behaviour that can be attributed to the numerous traps between not well-connected 3D islands forming the film.

Consistently with the structural and morphological findings highlighted above, upon thermal annealing V_{th} exhibits only a mild (positive) shift for PDI8CN2 devices whilst a remarkably large shift leading to a $V_{th} \sim 0$ V is observed in N1400 devices. This can be clearly ascribed to a better ability of the N1400 vs. PDI8CN2 molecules to re-assemble in a thermodynamically stable packing upon annealing. The post-annealing 2D fashion architecture of the N1400 certainly *heals* the various inter-grain traps centers giving rise to a large threshold voltage. Further, pre-annealing negative sign of V_{th} could stem from the above-mentioned inter-grain defects that require a higher gate voltage value in order to fill all the trap levels with electrons before a conductive channel is formed. Noteworthy, both molecules exhibit similar melting point temperatures ($\Delta T_m \sim 15$ °C) therefore the annealing experiments are comparable as performed at the same ΔT from the T_m of each

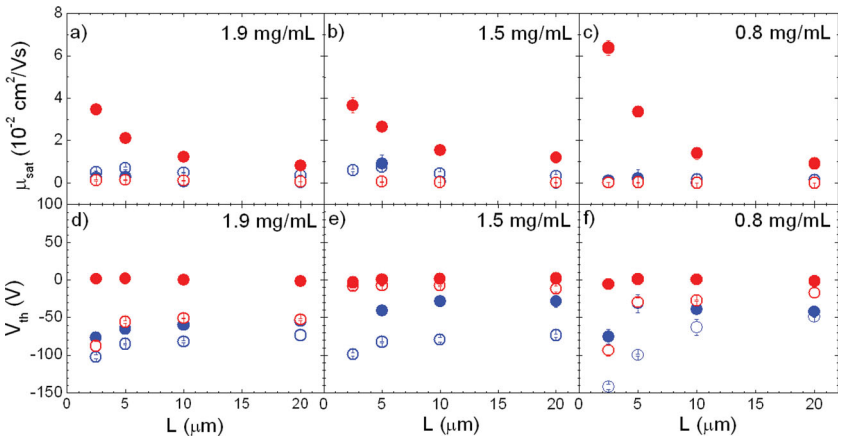

Figure 5. Plots of (a-c) μ_{sat} and (d-f) V_{th} vs. channel length (L) of thin-films spin-coated on HMDS-treated SiO_x. Blue and red circles refer to PDI8CN2 and N1400 devices, respectively. Empty and filled circles represent the as-cast devices and the devices after thermal annealing, respectively.

material. Interestingly, the mobility and threshold voltage variation upon annealing was not concentration-dependent as shown in Figure 5. For N1400, a steep decrease of the mobility with increasing the channel length is also observed which cannot be directly correlated with a contact resistance phenomenon. This latter would lead to a mobility decrease with decreasing L given that the channel resistance scales with L whilst the parasitic contact resistance component does not change with the channel length. We ascribed this trend to the increasing occurrence of grain-to-grain hopping events with the increasing the channel length; this is in line with AFM imaging observations revealing grain sizes typically exceeding 1 μm (after annealing). An additional improvement coming from a better reorganization of the N1400 molecules at the interface with the electrodes after the annealing step is represented by the disappearance of a parasitic resistive contribution that would manifest itself in the transfer curves at high (positive) gate voltages with an unexpected current decrease (see SI). In this region the undesired resistive contribution coming from the electrodes (R_c) can become comparable with the channel resistance (R_{ch}) that decreases with driving the device at progressively higher voltages after the V_{th} is reached. These two beneficial factors clearly dictate the improved performances of the branched-alkyl chains derivative with respect to PDI8CN2. An additional point can be made related to the more pronounced tendency of the threshold voltage to reduce upon increasing the channel length. As the inter-electrodic distance decreases, i.e. L becomes smaller, the corresponding charge density in the (bulk) region of the semiconductor between source and drain contact increases. Provided that charge density ρ and potential ϕ_s are linked by Poisson's equation, the injected amount of charges will induces shift in the electrostatic potential, which requires a compensation through a shift in V_{th} to shut the conduction off. Loosely speaking, to turn off the transistor, the space charge transferred from the electrodes into the bulk of the semiconductor needs to be compensated by an equal and opposite amount of charge accumulated in the channel which translates into a shift in V_{th}.

By and large, the improvement in the OFET performance for both molecules as a result of thermal annealing treatments can be clearly ascribed to the enhanced crystallinity within the films. However, such an improved performance in OFETs observed on the two different molecular films can be explained in view of two markedly different reasons. On the one hand in $PDI8CN_2$ films the crystalline grains increase in size and quality, reducing the grain boundaries density and thus the charge trapping; on the other hand the 3D morphology hinders the percolation between crystalline grains of two separated islands. This explains why after the annealing OFETs based on $PDI8CN_2$ show a mild improve. In contrast, the 2D morphology of N1400 films retain upon annealing allows the charge transport to percolate between the crystalline grains stabilized upon annealing. This is the reason of the strong improvement of the OFET characteristics in N1400 devices.

3. Conclusion

We have investigated the effect of alkyl side chains architecture of two perylene-diimide derivatives on structure, morphology and electrical properties of spin-coated films, and compared their performances after an annealing post-processing step. Both X-ray and spectroscopical investigations revealed that the substitution of linear side chains with branched ones, introduces four "distinct" stereoisomers, making the molecules more soluble and therefore increasing their processability. This configurational disorder *i)* makes the crystallization process more difficult with respect to the case of molecules with linear side-chains which self-assembles in the crystal structure optimal for charge transport; *ii)* favours the 2D-growth mode. These structural and morphological characteristics, ascribed to branched side chains, enable a phase transition by an ordinary post-deposition thermal treatment which strongly improves the transport properties of thin-film devices. These findings suggest that synthesizing highly processable molecules with strong supramolecular rearrangement capabilities during optimized classical post-growth processes can be more efficient than improving the charge carrier mobility at the expense of solubility. The annealing temperature at which the experiments were performed allows the full compatibility of the aforementioned post-deposition step even on plastic/flexible substrates whose thermal resistance does not typically exceed 180 °C. Furthermore, our study suggests that by mastering the molecular disorder of the active layer after deposition is key for ruling polaron transport in thin films of small semiconductive molecules.

4. Experimental Section

Materials: PDI8CN2 and N1400 molecules were used as received from Polyera and BASF, respectively.

Film Preparation: All the substrates (pre-patterned bottom gate-bottom contact devices with 230 nm of silicon oxide as dielectric, Fraunhofer IPMS, Dresden, Germany) were cleaned at ambient

conditions by acetone and isopropanol and then dried off using a gentle nitrogen flow. The device surface was functionalized by spin-coating 70 μL of HMDS to lower the electron trapping coming from the hydroxyl groups at the SiO_2 surface. Thin-films of PDI8CN2 and N1400 were prepared by spin-coating for 30 s at 1000 rpm 190 μL of solution in $CHCl_3$ onto the substrates. For each concentration considered two identical devices were prepared; the former was used as-prepared and the latter was first thermally annealed at 110 °C for 5 h. Both preparation and annealing were carried out in a N_2 environment.

Structural Characterization: 2D-GIXRD images were collected at the beamline XRD1 of ELETTRA synchrotron facility (Trieste, Italy) by using a wavelength of 1 Å and a beam size of 200 × 200 μm^2. The incident angle of the X-ray beam, α_i, was chosen below and close to the critical angle to discriminate the contribution to the diffraction pattern coming from the upper layers of the organic film and that coming from the substrate. The GIXRD diffraction patterns were recorded using a 2D camera (Pilatus detector) placed normal to the incident beam direction. XRR were performed using a SmartLab Rigaku diffractometer in a parallel beam geometry equipped with a $Cu_{K\alpha}$ (λ = 1.5418 Å) rotating anode followed by a parabolic mirror to collimate the incident beam and a series of variable slits (placed before and after the sample position) to obtain an acceptance of 0.02°.

The crystal structure of N1400 was retrieved by laboratory powder diffraction data, ab-initio indexing and structure solution and refinement methods, using a conventional Bragg-Brentano parafocussing geometry. Details in the structure solution and other crystallographic information are given in the Supplementary Information section.

CCDC 982087 contains the supplementary crystallographic data for this paper. These data can be obtained free of charge from The Cambridge Crystallographic Data Centre via www.ccdc.cam.ac.uk/data_request/cif.

Morphology: Topographical AFM characterization was carried out in intermittent contact mode in air environment making use of a Smena, NT-MDT (Moscow, Russia) and a Veeco Dimension 3100 operating on a Nanoscope IV control unit. Data analysis was performed using SPIP (Image Metrology) and Gwyddion softwares.

Electrical Characterization: Bottom-gate bottom-contact OFETs were electrically characterized in nitrogen atmosphere using a Keithley 2536A controlled by means of the LabTracer software. For each device several sets of both output and transfer curves were traced in the saturation and linear regime. The field-effect mobility was extracted through the fitting of the linear part of the sqrt(I_D) vs. V_{GS} curve in the saturation regime (V_{DS} = +80 V) using the following formula:

$$\mu = 2\left(\frac{\partial\sqrt{I_D}}{\partial V_{GS}}\right)^2 \frac{L}{WC_{ins}},$$

where W, L are the width and the length of the channel length, respectively, and C_{ins} (1.5×10^{-8} F/cm^2) is the silicon oxide capacitance (oxide thickness = 230 nm).

Supporting Information

Supporting Information is available from the Wiley Online Library or from the author.

Acknowledgements

The authors acknowledge Drs. S. Bonacchi, G. Nealon and J. A. Hutchison for helping with the absorption/emission and cyclic voltammetry experiments, Dr. L. Barba for technical support at the beamline. Dr. Silke Köhler (BASF Schweiz AG) for material supply, the Italian-French University for financial support under the grant of Vinci's program, the ERC project SUPRAFUNCTION (GA-257305), the EU Large Project One-P (FP7-NMP-2007–212311) and the International Center for Frontier Research in Chemistry (icFRC).

Received: March 10, 2014
Revised: May 2, 2014
Published online: July 8, 2014

[1] J. E. Anthony, A. Facchetti, M. Heeney, S. R. Marder, X. W. Zhan, *Adv. Mater.* **2010**, *22*, 3876.
[2] A. Dodabalapur, *Nature* **2005**, *434*, 151.
[3] H. Yan, Y. Zheng, R. Blache, C. Newman, S. F. Lu, J. Woerle, A. Facchetti, *Adv. Mater.* **2008**, *20*, 3393.
[4] B. Yoo, T. Jung, D. Basu, A. Dodabalapur, B. A. Jones, A. Facchetti, M. R. Wasielewski, T. J. Marks, *Appl. Phys. Lett.* **2006**, *88*, 082104.
[5] C. Kim, A. Facchetti, T. J. Marks, *Science* **2007**, *318*, 76.
[6] M. Novak, A. Ebel, T. Meyer-Friedrichsen, A. Jedaa, B. F. Vieweg, G. A. Yang, K. Voitchovsky, F. Stellacci, E. Spiecker, A. Hitsch, M. Halik, *Nano Lett.* **2011**, *11*, 156.
[7] M. A. McCarthy, B. Liu, E. P. Donoghue, I. Kravchenko, D. Y. Kim, F. So, A. G. Rinzler, *Science* **2011**, *332*, 570.
[8] M. E. Roberts, S. C. B. Mannsfeld, N. Queralto, C. Reese, J. Locklin, W. Knoll, Z. N. Bao, *Proc. Natl. Acad. Sci. USA* **2008**, *105*, 12134.
[9] S. Colella, C. Ruzie, G. Schweicher, J. B. Arlin, J. Karpinska, Y. Geerts, P. Samorì, *ChemPlusChem* **2014**, *79*, 371.
[10] OLED displays are integrated in Samsung products (e.g., Galaxy S4 smartphone, OLED TV-TM)
[11] X. L. Feng, V. Marcon, W. Pisula, M. R. Hansen, J. Kirkpatrick, F. Grozema, D. Andrienko, K. Kremer, K. Müllen, *Nature Mater.* **2009**, *8*, 421.
[12] H. Usta, C. Risko, Z. M. Wang, H. Huang, M. K. Deliomeroglu, A. Zhukhovitskiy, A. Facchetti, T. J. Marks, *J. Am. Chem. Soc.* **2009**, *131*, 5586.
[13] M. Cavallini, C. Albonetti, F. Biscarini, *Adv. Mater.* **2009**, *21*, 1043.
[14] Z. Bao, J. Locklin, *Organic Field Effect Transistors*, CRC Press, Boca Raton **2007**.
[15] C. Wöll, *Physical and Chemical Aspects of Organic Electronic*, Wiley-VCH, Weinheim **2009**.
[16] G. De Luca, W. Pisula, D. Credgington, E. Treossi, O. Fenwick, G. M. Lazzerini, R. Dabirian, E. Orgiu, A. Liscio, V. Palermo, K. Müllen, F. Cacialli, P. Samorì, *Adv. Funct. Mater.* **2011**, *21*, 1279.
[17] V. Palermo, P. Samorì, *Angew. Chem. Int. Ed.* **2007**, *46*, 4428.
[18] D. M. De Leeuw, M. M. J. Simenon, A. R. Brown, R. E. F. Einerhand, *Synthetic Met.* **1997**, *87*, 53.
[19] B. A. Jones, A. Facchetti, M. R. Wasielewski, T. J. Marks, *J. Am. Chem. Soc.* **2007**, *129*, 15259.
[20] R. Schmidt, J. H. Oh, Y. S. Sun, M. Deppisch, A. M. Krause, K. Radacki, H. Braunschweig, M. Konemann, P. Erk, Z. A. Bao, F. Würthner, *J. Am. Chem. Soc.* **2009**, *131*, 6215.
[21] C. Piliego, D. Jarzab, G. Gigli, Z. H. Chen, A. Facchetti, M. A. Loi, *Adv. Mater.* **2009**, *21*, 1573.
[22] R. T. Weitz, K. Amsharov, U. Zschieschang, E. B. Villas, D. K. Goswami, M. Burghard, H. Dosch, M. Jansen, K. Kern, H. Klauk, *J. Am. Chem. Soc.* **2008**, *130*, 4637.
[23] Y. G. Wen, Y. Q. Liu, *Adv. Mater.* **2010**, *22*, 1331.
[24] C. Piliego, F. Cordella, D. Jarzab, S. Lu, Z. Chen, A. Facchetti, M. A. Loi, *Appl. Phys. A-Mater.* **2009**, *95*, 303.
[25] M. L. Tang, J. H. Oh, A. D. Reichardt, Z. N. Bao, *J. Am. Chem. Soc.* **2009**, *131*, 3733.
[26] J. Rivnay, L. H. Jimison, J. E. Northrup, M. F. Toney, R. Noriega, S. F. Lu, T. J. Marks, A. Facchetti, A. Salleo, *Nature Mater.* **2009**, *8*, 952.
[27] J. M. Mativetsky, E. Orgiu, I. Lieberwirth, W. Pisula, P. Samorì, *Adv. Mater.* **2014**, *26*, 430.

[28] N. S. An, Y. N. Shi, J. Q. Feng, D. P. Li, J. Gao, Y. L. Chen, X. Y. Li, *Org. Electron.* **2013**, *14*, 1197.
[29] R. C. Savage, E. Orgiu, J. M. Mativetsky, W. Pisula, T. Schnitzler, C. L. Eversloh, C. Li, K. Müllen, P. Samorì, *Nanoscale* **2012**, *4*, 2387.
[30] P. Samorì, A. Fechtenkötter, F. Jäckel, T. Böhme, K. Müllen, J. P. Rabe, *J. Am. Chem. Soc.* **2001**, *123*, 11462.
[31] K. Balakrishnan, A. Datar, T. Naddo, J. L. Huang, R. Oitker, M. Yen, J. C. Zhao, L. Zang, *J. Am. Chem. Soc.* **2006**, *128*, 7390.
[32] F. J. Zhang, Y. B. Hu, T. Schuettfort, C. A. Di, X. K. Gao, C. R. McNeill, L. Thomsen, S. C. B. Mannsfeld, W. Yuan, H. Sirringhaus, D. B. Zhu, *J. Am. Chem. Soc.* **2013**, *135*, 2338.
[33] F. Liscio, C. Albonetti, K. Broch, A. Shehu, S. D. Quiroga, L. Ferlauto, C. Frank, S. Kowarik, R. Nervo, A. Gerlach, S. Milita, F. Schreibers, F. Biscarini, *ACS Nano* **2013**, *7*, 1257.
[34] F. Liscio, S. Milita, C. Albonetti, P. D'Angelo, A. Guagliardi, N. Masciocchi, R. G. Della Valle, E. Venuti, A. Brillante, F. Biscarini, *Adv. Funct. Mater.* **2012**, *22*, 943.
[35] B. A. Jones, A. Facchetti, M. R. Wasielewski, T. J. Marks, *Adv. Funct. Mater.* **2008**, *18*, 1329.
[36] M. Cavallini, P. D'Angelo, V. V. Criado, D. Gentili, A. Shehu, F. Leonardi, S. Milita, F. Liscio, F. Biscarini, *Adv. Mater.* **2011**, *23*, 5091.
[37] I. Bar, J. Bernstein, *J. Phys. Chem.* **1982**, *86*, 3223.
[38] C. P. Brock, J. D. Dunitz, *Chem. Mater.* **1994**, *6*, 1118.
[39] P. Zugenmaier, J. Duff, T. L. Bluhm, *Cryst. Res. Technol.* **2000**, *35*, 1095.
[40] M. C. R. Delgado, E. G. Kim, D. A. da Silva, J. L. Brédas, *J. Am. Chem. Soc.* **2010**, *132*, 3375.
[41] A. Fechtenkötter, N. Tchebotareva, M. Watson, K. Müllen, *Tetrahedron* **2001**, *57*, 3769.
[42] H. Lorenz, A. Seidel-Morgenstern, *Thermochim. Acta* **2002**, *382*, 129.
[43] G. Giannini, F. Cuppo, L. Fontanive, N. D'Amelio, A. Cesaro, A. Maiocchi, F. Uggeri, *J. Therm. Anal. Calorim.* **2011**, *103*, 89.
[44] L. L. Chua, J. Zaumseil, J. F. Chang, E. C. W. Ou, P. K. H. Ho, H. Sirringhaus, R. H. Friend, *Nature* **2005**, *434*, 194.
[45] D. T. Duong, M. F. Toney, A. Salleo, *Phys. Rev. B* **2012**, *86*, 205205.
[46] B. E. Warren, *X-ray Diffraction*, Dover, New York **1990**.
[47] D. M. Smilgies, *J. Appl. Crystallogr.* **2009**, *42*, 1030.
[48] H. Kiessig, *Ann. Phys.* **1931**, *10*, 769.
[49] P. Colombi, D. K. Agnihotri, V. E. Asadchikov, E. Bontempi, D. K. Bowen, C. H. Chang, L. E. Depero, M. Farnworth, T. Fujimoto, A. Gibaud, M. Jergel, M. Krumrey, T. A. Lafford, A. Lamperti, T. Ma, R. J. Matyi, M. Meduna, S. Milita, K. Sakurai, L. Shabel'nikov, A. Ulyanenkov, A. Van der Lee, C. Wiemer, *J. Appl. Crystallogr.* **2008**, *41*, 143.
[50] L. Parratt, *Phys. Rev.* **1954**, *95*, 359.
[51] C. V. Thompson, *Ann. Rev. Mater. Res.* **2012**, *42*, 399.